nature Accelerated Article Preview

LETTER
doi:10.1038/nature26154

Correlated insulator behaviour at half-filling in magic-angle graphene superlattices

Yuan Cao, Valla Fatemi, Ahmet Demir, Shiang Fang, Spencer L. Tomarken, Jason Y. Luo, J. D. Sanchez-Yamagishi, K. Watanabe, T. Taniguchi, E. Kaxiras, R. C. Ashoori & P. Jarillo-Herrero

Cite this article as: Cao, Y. *et al.* Correlated insulator behaviour at half-filling in magic-angle graphene superlattices. *Nature* http://dx.doi.org/10.1038/nature26154 (2018).

Received 6 October 2017; accepted 21 February 2018.
Accelerated Article Preview Published online 5 March 2018.

LETTER

doi:10.1038/nature26154

Correlated insulator behaviour at half-filling in magic-angle graphene superlattices

Yuan Cao[1], Valla Fatemi[1], Ahmet Demir[1], Shiang Fang[2], Spencer L. Tomarken[1], Jason Y. Luo[1], J. D. Sanchez-Yamagishi[2], K. Watanabe[3], T. Taniguchi[3], E. Kaxiras[2,4], R. C. Ashoori[1] & P. Jarillo-Herrero[1]

van der Waals heterostructures are an emergent class of metamaterials that consist of vertically stacked two-dimensional building blocks, which provide us with a vast tool set to engineer their properties on top of the already rich tunability of two-dimensional materials.[1] One of the knobs, the twist angle between different layers, has a crucial role in the ultimate electronic properties of a van der Waals heterostructure and does not have a direct analogue in other systems such as MBE-grown semiconductor heterostructures. For small twist angles, the moiré pattern that is produced by the lattice misorientation creates a long-range modulation. So far, the study of the effect of twist angles in van der Waals heterostructures has been mostly concentrated in graphene/hexagonal boron nitride twisted structures, which exhibit relatively weak interlayer interaction owing to the presence of a large bandgap in hexagonal boron nitride.[2–5] Here we show experimentally that when two graphene sheets are twisted by an angle close to the theoretically predicted 'magic angle' the resulting band structure near charge neutrality becomes flat owing to the strong interlayer coupling.[6] These flat bands exhibit insulating phases at half-filling, which are not expected in a non-interacting picture. We show that the half-filling states are consistent with a Mott-like insulator state that can arise from electrons localized in the moiré superlattice. These unique properties of magic-angle twisted bilayer graphene may open a new playground for exotic many-body quantum phases in a two-dimensional platform without magnetic field. The easy accessibility of the flat bands, the electrical tunability, and the bandwidth tunability though twist angle may pave the way towards more exotic correlated systems, such as unconventional superconductors or quantum spin liquids.

Exotic quantum phenomena often occur in condensed matter and other systems with high density of states. Remarkable examples include superconductivity and the fractional quantum hall effect. One way of creating high density of states is to have flat bands with weak dispersion in momentum space, where the electron kinetic energy is set by the bandwidth W. When the Fermi level lies within the flat bands, Coulomb interactions (U) can then greatly exceed the kinetic energy of the electrons and drive the system into various strongly correlated phases ($U/W \gg 1$).[7–11] The study of such flat-band systems in bulk materials continues to be scientifically important, and the search for new flat-band systems, such as in kagome and Lieb lattices as well as in heavy fermion systems, is ongoing.[7–12]

Recent advances in two-dimensional materials provide a new route for achieving flat bands. An inherent advantage in two-dimensional is that the chemical potential of electrons can be continuously tuned via electric field effect without introducing extra disorder. In a twisted van der Waals heterostructure, the mismatch between two similar lattices generates a moiré pattern (Fig. 1b). This additional periodicity, which can have a length scale orders of magnitude larger than the underlying atomic lattices, has been shown to create a fractal energy spectrum in a strong magnetic field.[2–4] In twisted layers, the interlayer hybridization is modulated by the moiré pattern as well. As an example, the band structure of TBG can be tailored to generate band gaps and band curvatures otherwise absent in the graphene bands.[6,13–17] Although the well-known building blocks for van der Waals heterostructures, such as graphene and transition metal dichalcogenides, do not have intrinsic flat bands at low energies, it has been predicted theoretically that flat bands may exist in TBG.[6,14–16,18] In this work, we demonstrate experimentally that when the twist angle of TBG is close to the theoretically predicted 'magic angle', the interlayer hybridization induces nearly-flat low-energy bands. This quenching of the quantum kinetic energy leads to a correlated insulating phase at half-filling of these flat bands, which points towards a Mott-like insulator in the localized flat bands.

To zeroth order, the low energy band structure of TBG can be considered as two sets of monolayer graphene Dirac cones rotated about the Γ point by the twist angle θ (Fig. 1d).[6] The difference between the two K (or K') wave vectors gives rise to the mini Brillouin zone (MBZ), shown as a small hexagon, which is reciprocal to the moiré superlattice. The Dirac cones near the same valley mix through interlayer hybridization, while interactions between distant Dirac cones are exponentially suppressed.[6,13] As a result, the valley itself remains (for all practical purposes) a good quantum number. Two experimentally verified consequences of this hybridization are energy gaps that open near the intersection of the Dirac cones and renormalization of the Fermi velocity

$$v_F = \frac{1}{\hbar} |\nabla_{\boldsymbol{k}} E_{\boldsymbol{k}}|_{\boldsymbol{k}=K,K'}$$

at the Dirac points.[13,19–21]

The theoretically calculated 'magic angles' $\theta^{(i)}_{\text{magic}}$, $i = 1, 2, \ldots$ are a series of twist angles at which the Fermi velocity at the Dirac points becomes zero.[6] The resulting low-energy bands near these twist angles are confined to less than about 10 meV. These phenomena can be qualitatively understood from the competition between the kinetic energy and interlayer hybridization energy (Fig. 1e-g). Intuitively, when the hybridization energy $2w$ is comparable or larger than $\hbar v_0 k_\theta$ where $v_0 = 10^6\,\text{m s}^{-1}$ is the Fermi velocity of graphene and $k_\theta \approx K\theta$ is the momentum displacement of the Dirac cones, the lower of the hybridized states is pushed to and crosses zero energy. A detailed treatment gives the first magic angle $\theta^{(1)}_{\text{magic}} = \sqrt{3}\,w/(\hbar v_0 K)$, which is approximately 1.1°.[6] Fig. 1c shows an *ab initio* tight-binding calculation of the band structure for $\theta = 1.08°$.[16] The labeled flat bands have a bandwidth of 12 meV for the $E > 0$ branch and 2 meV for the $E < 0$ branch. From a band theory point of view, the flat bands should have localized wave function profiles in real space. Figure 1h shows the calculated local density of states for the flat bands. The wave functions are indeed highly concentrated in the regions with AA stacking, while small but finite amplitudes on the AB and BA regions connect the AA regions and

[1]Department of Physics, Massachusetts Institute of Technology, Cambridge, Massachusetts 02139, USA. [2]Department of Physics, Harvard University, Cambridge, Massachusetts 02138, USA. [3]National Institute for Materials Science, Namiki 1-1, Tsukuba, Ibaraki 305-0044, Japan. [4]John A. Paulson School of Engineering and Applied Sciences, Harvard University, Cambridge, Massachusetts 02138, USA.

endow a weak dispersion to the bands.[6, 15, 18] A brief discussion about the topological structure of the bands near the first magic angle is given in Methods and Extended Data Fig. 1.

For the experiment, we fabricated high-quality encapsulated TBG devices with twist angle precisely controlled to about 0.1°–0.2° accuracy using a previously developed 'tear and stack' technique.[13,17,22] We have measured four devices that have twist angles near the first magic angle $\theta^{(1)}_{\mathrm{magic}} \approx 1.1°$. Fig. 2a shows the low-temperature two-probe conductance of device D1 as a function of carrier density n. Near $n = \pm n_s = \pm 2.7 \times 10^{12}\,\mathrm{cm}^{-2}$ ($4e^-$ per moiré unit cell for the twist angle $\theta = 1.08°$), the conductance is zero over a wide range of densities. These insulating states have been previously understood as hybridization induced band gaps above and below the lowest energy superlattice bands, and will be hereafter referred to as the 'superlattice gaps'.[13] The measured thermal activation gaps are about 40 meV.[13,17] The twist angle can be estimated from the density required to reach the superlattice gaps, which we find to be $\theta = 1.1° = 0.1°$ for all of the devices reported here.

A new pair of insulating phases occurs for a narrower density range near half of the superlattice density $n = \pm n_s/2 = \pm 1.4 \times 10^{12}\,\mathrm{cm}^{-2}$ ($2e^-$ per moiré unit cell). These insulating states have a much smaller energy scale. Note that this behaviour is markedly different from all other zero-field insulating behaviours previously reported in the recent literature (which occur at either $\pm n_s$ or at an integer multiple of $\pm n_s$), and we shall refer to them as half-filling insulating states.[13,17] These states are observed at roughly the same density for all four devices (Fig. 2a inset). Fig. 2b–d show the conductance of the half-filling states in device D1 at different temperatures. Above 4 K, the system behaves as a metal, exhibiting decreasing conductance with increasing temperature. A metal-insulator transition occurs near 4 K. The conductance drops significantly from 4 K to 0.3 K, with the minimum value decreasing by 1.5 orders of magnitude. An Arrhenius fit gives a thermal activation gap of about 0.3 meV for the half-filling states, two orders of magnitude smaller than those of the superlattice gaps. At the lowest temperatures the system may be limited by conduction through charge puddles, resulting in deviation from the Arrhenius fit.

To confirm the existence of the half-filling states, we performed capacitance measurements on device D2 using an ac low-temperature capacitance bridge (see Extended Figure 2).[23] The real and imaginary components of the ac measurement give information about the change in capacitance and the loss tangent of the device, respectively. The latter signal is tied to the dissipation in the device due to its resistance.[23] Device D2 exhibits a reduction in capacitance and strong enhancement of dissipation at $\pm n_s/2$ as shown in Fig. 3a, in agreement with an insulating phase that results from the suppression in density of states. The insulating state at $-n_s/2$ is weaker and only visible in the dissipation data. The observation of capacitance reduction (i.e. suppression of density of states) for only the n-side half-filling state in this device may be due to an asymmetric band structure and/or device quality. The reduction (enhancement) in capacitance (dissipation) vanishes when the device is warmed up from 0.3 K to about 2 K, consistent with the behavior observed in transport measurements.

The emergence of half-filling states is not expected in a single-particle picture and appears to be correlated with the narrow bandwidth near the first magic angle. In our experiment, several separate pieces of evidence support the presence of flat bands. First, we measured the temperature dependence of the amplitude of Shubnikov–de Haas (SdH) oscillations in device D1, from which we extracted the electron effective mass m^* (Fig. 3b, see Methods and Extended Data Figure 3 for analysis). For a Dirac spectrum with eight-fold degeneracy (spin, valley, and layer), one would expect that $m^* = \sqrt{\hbar^2 n/(8\pi v_F^2)}$ which scales as $1/v_F$. The large measured m^* near charge neutrality in device D1 indicates a 25-fold reduction in v_F ($v_F = 4 \times 10^4\,\mathrm{m\,s}^{-1}$, compared to $10^6\,\mathrm{m\,s}^{-1}$ in monolayer graphene). This striking reduction of the Fermi velocity is an expected characteristic of the flat bands. Furthermore, we analyzed the capacitance data of device D2 near the Dirac point (Fig. 3a), finding that a Fermi velocity reduced to about $0.15v_0$ is necessary for a good fit to the data (see Methods and Extended Data Figure 1b). Finally, another direct manifestation of such flat bands is the flattening of the conductance minimum at charge neutrality above a temperature of 40 K ($kT = 3.5$ meV), as seen in Fig. 3c. While the conductance minimum in monolayer graphene can be clearly observed even near room temperature, it is smeared out in magic-angle twisted bilayer grapheme (MA-TBG) when the thermal energy kT becomes comparable to $v_F k_\theta/2 \approx 4$ meV, the energy scale spanning the Dirac-like portion of the band (see Fig. 1c).[24-26]

Due to the localized nature of the electrons, a plausible explanation for the gapped behavior at half-filling is the formation of a Mott-like insulator driven by Coulomb interaction between electrons.[27,28] To this end, we can consider a Hubbard model on a triangular lattice, where each site corresponds to a localized region with AA stacking in the moiré pattern (Fig. 1i). Fig. 3d shows the numerically calculated bandwidth of the E>0 branch of the low-energy bands for $0.04° < \theta < 2°$ using a continuum model of TBG.[6] The bandwidth W is strongly suppressed near the magic angles. The on-site Coulomb energy U of each site is estimated as $e^2/(4\pi\varepsilon d)$, in which d is the effective linear dimension of each site (with the same length scale as the moiré period) and ε is the effective dielectric constant including screening. Absorbing ε and the dependence of d on twist angle into a single constant κ, we can write $U = e^2\theta/(4\pi\varepsilon_0\kappa a)$ ($a = 0.246$ nm is the lattice constant of monolayer graphene). In Fig. 3d we plot the on-site energy U versus θ for $\kappa = 4$–20. As a reference, $\kappa = 4$ if one assumes $\varepsilon = 10\varepsilon_0$ and d equals 40% of the moiré wavelength. For a range of possible values of κ it is therefore reasonable that $U/W > 1$ occurs near the magic angles and results in half-filling Mott-like gaps.[27] The realistic scenario is however much more complicated than these simplistic estimates and will require detailed theoretical analysis of the interactions responsible for the correlated gaps.

The SdH oscillation frequency, shown on the right-hand axis of Fig. 3b, also supports the existence of Mott-like correlated gaps at half-filling. Near the charge neutrality point, the oscillation frequency closely follows $f_{\mathrm{SdH}} = \phi_0|n|/N$ where $\phi_0 = h/e$ is the flux quantum and $N = 4$ indicates the spin and valley degeneracies. Surprisingly, at $|n| > n_s/2$ we observe oscillation frequencies that corresponds to straight lines $f_{\mathrm{SdH}} = \phi_0(|n| - n_s/2)/N$ in which N has a reduced value of 2. Moreover, these lines extrapolate to zero exactly at the densities of the half-filling states at $n = \pm n_s/2$. These oscillations point towards small Fermi pockets that result from doping the half-filling states, which might originate from charged quasiparticles near a Mott-like insulator phase.[29] The halved degeneracy of the Fermi pockets might be related to the spin-charge separation predicted in a Mott insulator.[29] These results are also supported by Hall measurements at 0.3 K presented in Extended Data Figure 4 (see Methods for discussion), that show a 'resetting' of the Hall densities when the system is electrostatically doped beyond the Mott-like states.

The half-filling states at $\pm n_s/2$ are suppressed by the application of a magnetic field. Figure 4a-b shows that both insulating phases start to conduct at a perpendicular field of $B = 4$ T and recover normal conductance by $B = 8$ T. A similar effect is observed for in-plane magnetic field (see Extended Data Figure 5d). The insensitivity to field orientation suggests the suppression of the half-filling states is due to a Zeeman effect rather than an orbital effect, as the latter would be affected only by the perpendicular component of the magnetic field. For an effective g-factor $g = 2$ due to electron spin, the Zeeman energy needed to suppress the half-filling states is approximately $g\mu_B B = 0.5$ meV, of the same order as the thermal excitation energy scale.

Our data point towards the presence of a spin-singlet Mott-like insulator ground state at half-filling and zero magnetic field (Fig. 4e). The application of an external magnetic field can possibly polarize the excitations in the spectrum of the correlated states according to their spin. When the Zeeman energy exceeds the charge gap, charge conduction can therefore occur (Fig. 4f). In a typical Mott insulator, the ground state usually has an antiferromagnetic spin ordering below the Néel

temperature. On a triangular lattice, however, the frustration prevents the fully anti-parallel alignment of adjacent spins. Possible ordering schemes include 120° Néel order and rotational symmetry breaking stripe order.[30] It is yet unclear whether the spin-singlet ground state in MA-TBG is fulfilled by any of the above ordering schemes or simply disordered at low temperatures. In the half-filling states of MA-TBG it is also possible that the ordering, if any, occurs in conjunction with the valley degree of freedom. Therefore, a complete theoretical treatment of this problem should at least involve considering a two-band Hubbard model on a triangular lattice.

We also comment on other competing mechanisms for creating a half-filled insulating state in a system with flat bands. Among the possibilities, charge density waves in two-dimensional are often stabilized by Fermi surface nesting, which can in principle occur near the half-filling of a two-dimensional Brillouin zone.[31] However, the nesting is not sufficient to fully gap out the entire Fermi surface to achieve an insulating state. In order to create a global gap at half-filling, at least a doubling of the unit cell would be necessary, which could be created by a commensurate charge density wave or lattice relaxation due to strain. Scanning tunneling microscopy conducted at temperatures below 4 K may be able to differentiate such mechanisms.

In summary, our work demonstrates that graphene can be transformed through van der Waals engineering into a flat-band system where novel insulating states at half-filling are present. These insulating states cannot be explained by a simple non-interacting picture, and point towards the importance of correlations in this flat-band system. However, we note that the lattice and electronic structure near MA-TBG superlattices is very complex and further theoretical and experimental work will be fundamental to fully ascertain the importance of correlation effects. Through its easy gate tunability, MA-TBG could thus provide a novel playground for studying the transition between a correlated metal and an interaction-driven insulating state, which may provide insight into strongly-correlated materials, notably high-temperature superconductivity. The richness of the combined spin and valley degrees of freedom on a triangular lattice could also give rise to other exotic quantum phases such as quantum spin liquids.[32]

Online Content Methods, along with any additional Extended Data display items and Source Data, are available in the online version of the paper; references unique to these sections appear only in the online paper.

Received 6 October 2017; accepted 21 February 2018.
Published online 5 March 2018.

1. Geim, A. K. & Grigorieva, I. V., Van der Waals heterostructures. *Nature* **499**, 419–425 (2013).
2. Hunt, B. *et al.*, Massive Dirac Fermions and Hofstadter Butterfly in a van der Waals Heterostructure. *Science* **340**, 1427–1430 (2013).
3. Dean, C. R. *et al.*, Hofstadter's butterfly and the fractal quantum Hall effect in moiré superlattices. *Nature* **497**, 598–602 (2013).
4. Ponomarenko, L. A. *et al.*, Cloning of Dirac Fermions in graphene superlattices. *Nature* **497**, 594–597 (2013).
5. Song, J. C. W., Shytov, A. V. & Levitov, L. S., Electron Interactions and Gap Opening in Graphene Superlattices. *Phys. Rev. Lett.* **111**, 266801 (2013).
6. Bistritzer, R. & MacDonald, A. H., Moiré bands in twisted double-layer graphene. *Proc. Natl. Acad. Scie. U. S. A.* **108(30)**, 12233–12237 (2011).
7. Wu, C., Bergman, D., Balents, L. & Das Sarma, S., Flat Bands and Wigner Crystallization in the Honeycomb Optical Lattice. *Phys. Rev. Lett.* **99**, 070401 (2007).
8. Iglovikov, V. I., Hèbert, F., Grèmaud, B., Batrouni, G. G. & Scalettar, R. T., Superconducting transitions in flat-band systems. *Phys. Rev. B* **094506**, 90 (2014).
9. Tsai, W. F., Fang, C., Yao, H. & Hu, J., Interaction-driven topological and nematic phases on the Lieb lattice. *New J. Phys.* **17**, 055016 (2015).
10. Lieb, E. H., Two theorems on the Hubbard model. *Phys. Rev. Lett.* **62**, 1201 (1989).
11. Mielke, A., Exact ground states for the Hubbard model on the Kagome lattice. *J. Phys. A* **25**, 4335–4345 (1992).
12. Si, Q. & Steglich, F., Heavy Fermions and Quantum Phase Transitions. *Science* **329**, 1161 (2010).
13. Cao, Y. *et al.*, Superlattice-induced insulating states and valley-protected orbits in twisted bilayer graphene. *Phys. Rev. Lett.* **117**, 116804 (2016).
14. Morell, E. S., Correa, J. D., Vargas, P., Pacheco, M. & Barticevic, Z., Flat bands in slightly twisted bilayer graphene: Tight-binding calculations. *Phys. Rev. B* **82**, 121407 (2010).
15. dos Santos, J. M. B. L., Peres, N. M. R. & Castro Neto, A. H., Continuum model of the twisted graphene bilayer. *Phys. Rev. B* **86**, 155449 (2012).
16. Fang, S. & Kaxiras, E., Electronic structure theory of weakly interacting bilayers. *Phys. Rev. B* **93**, 235153 (2016).
17. Kim, K. *et al.*, Tunable moiré bands and strong correlations in small-twist-angle bilayer graphene. *Proc. National Acad. Sci. U. S. A.* **114**, 3364 (2017).
18. de Laissardiére, G. T., Mayou, D. & Magaud, L., Numerical studies of confined states in rotated bilayers of graphene. *Phys. Rev. B* **125413**, 86 (2012).
19. Li, G. *et al.*, Observation of Van Hove singularities in twisted graphene layers. *Nat. Phys.* **6**, 109 (2010).
20. Luican, A. *et al.*, Single-Layer Behavior and Its Breakdown in Twisted Graphene Layers. *Phys. Rev. Lett.* **106**, 126802 (2011).
21. Brihuega, I. *et al.*, Unraveling the Intrinsic and Robuts Nature of van Hove Singularities in Twisted Bilayer Graphene by Scanning Tunneling Microscopy and Theoretical Analysis. *Phys. Rev. Lett.* **109**, 196802 (2012).
22. Kim, K. *et al.*, van der Waals Heterostructures with High Accuracy Rotational Alignment. *Nano Lett.* **16**, 1989 (2016).
23. Ashoori, R. C. *et al.*, Single-electron capacitance spectroscopy of discrete quantum levels. *Phys. Rev. Lett.* **68**, 3088 (1996).
24. Novoselov, K. S. *et al.*, Electric Field Effect in Atomically Thin Carbon Films. *Science* **306**, 666 (2004).
25. Morozov, S. V. *et al.*, Giant intrinsic carrier mobilities in graphene and its bilayer. *Phys. Rev. Lett.* **100**, 016602 (2008).
26. Bolotin, K. I., Sikes, K. J., Hone, J., Stormer, H. L. & Kim, P., Temperature-Dependent Transport in Suspended Graphene. *Phys. Rev. Lett.* **101**, 096802 (2008).
27. Mott, N. F., *Metal-Insulator Transitions* (Taylor and Francis, London/Philadelphia, 1990).
28. Imada, M., Fujimori, A. & Tokura, Y., Metal-insulator transitions. *Rev. Mod. Phys.* **70**, 1039 (1998).
29. Lee, P. A., Nagaosa, N. & Wen, X.-G., Doping a Mott insulator: Physics of high-temperature superconductivity. *Rev. Mod. Phys.* **78**, 17 (2006).
30. Misumi, K., Kaneko, T. & Ohta, Y., Mott transition and magnetism of the triangular-lattice Hubbard model with next-nearest-neighbor hopping. *Phys. Rev. B* **95**, 075124 (2017).
31. Grüner, G., *Density Waves In Solids* (Westview Press, 2009).
32. Balents, L., Spin liquids in frustrated magnets. *Nature* **464**, 199–208 (2010).

Acknowledgements We acknowledge discussions with L. Levitov, P. Lee, S. Todadri, B. I. Halperin, S. Carr, Z. Alpichshev, J. Y. Khoo and N. Staley. This work has been primarily supported by the National Science Foundation (DMR-1405221) and Gordon and Betty Moore Foundation's EPiQS Initiative through Grant GBMF4541 for device fabrication, transport measurements, and data analysis (Y.C., J.Y.L., J.D.S-Y., P.J.H.), with additional support from the NSS Program, Singapore (J.Y.L.). Capacitance work by R.A., A.D., and S.L.T. and theory work by S.F. has been supported by the STC Center for Integrated Quantum Materials, NSF Grant No. DMR-1231319. Data analysis by V.F. has been supported by AFOSR grant No. FA9550-16-1-0382. K.W. and T.T. acknowledge support from the Elemental Strategy Initiative conducted by the MEXT, Japan and JSPS KAKENHI Grant Numbers JP15K21722 and JP25106006. This work made use of the Materials Research Science and Engineering Center Shared Experimental Facilities supported by the National Science Foundation (DMR-0819762) and of Harvard's Center for Nanoscale Systems, supported by the NSF (ECS-0335765). E.K. acknowledges support by ARO MURI Award W911NF-14-0247.

Author Contributions Y.C., J.Y.L., J.D.S-Y fabricated the devices and performed transport measurements. Y.C., V.F. performed data analysis. P.J.H. supervised the project. S.F. and E.K. provided numerical calculations. S.L.T., A.D. and R.C.A. measured capacitance data. K.W. and T.T. provided hexagonal boron nitride devices. Y.C., V.F., and P.J.H. wrote the paper with input from all authors.

Author Information Reprints and permissions information is available at www.nature.com/reprints. The authors declare no competing financial interests. Readers are welcome to comment on the online version of the paper. Publisher's note: Springer Nature remains neutral with regard to jurisdictional claims in published maps and institutional affiliations. Correspondence and requests for materials should be addressed to P.J.-H. (pjarillo@mit.edu).

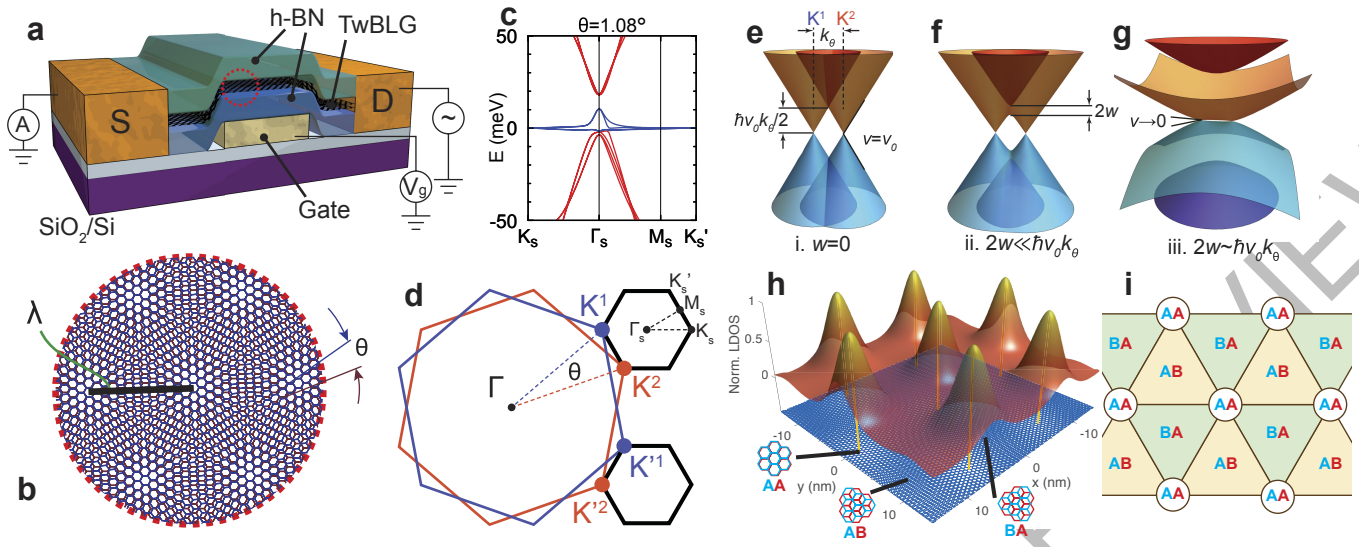

Figure 1 | Electronic band structure of twisted bilayer graphene (TBG). (a) Schematic of the TBG devices. The TBG is encapsulated in hexagonal boron nitride flakes of about 10–30-nm thickness. The conductance is measured with a voltage bias of 100 μV while varying the local bottom gate voltage. (b) The moiré pattern as seen in TBG. The moiré wavelength $\lambda = a/[2\sin(\theta/2)]$ where $a = 0.246$ nm is the lattice constant of graphene and θ is the twist angle. (c) The band structure of $\theta = 1.08°$ magic-angle TBG (MA-TBG) calculated with an *ab initio* tight-binding method. The bands shown in blue are the flat bands under study in this work. (d) The mini Brillouin zone (MBZ) is constructed from the difference between the two K (K') wave vectors from the two layers. Hybridization occurs between Dirac cones within each valley, while intervalley processes are strongly suppressed. (e-g) Illustration of the effect of interlayer hybridization for (e) $w = 0$, (f) $2w \ll \hbar v_0 k_\theta$ and (g) $2w \approx \hbar v_0 k_\theta$. (h) Calculated local density of states (LDOS) for the flat bands with $E > 0$ at $\theta = 1.08°$. The electron density is strongly concentrated at the regions with A–A stacking order, while mostly depleted at A–B and B–A stacked regions. See Extended Data Fig. 6 for density of states versus energy at the same twist angle. (i) Top view of a simplified model of the stacking order.

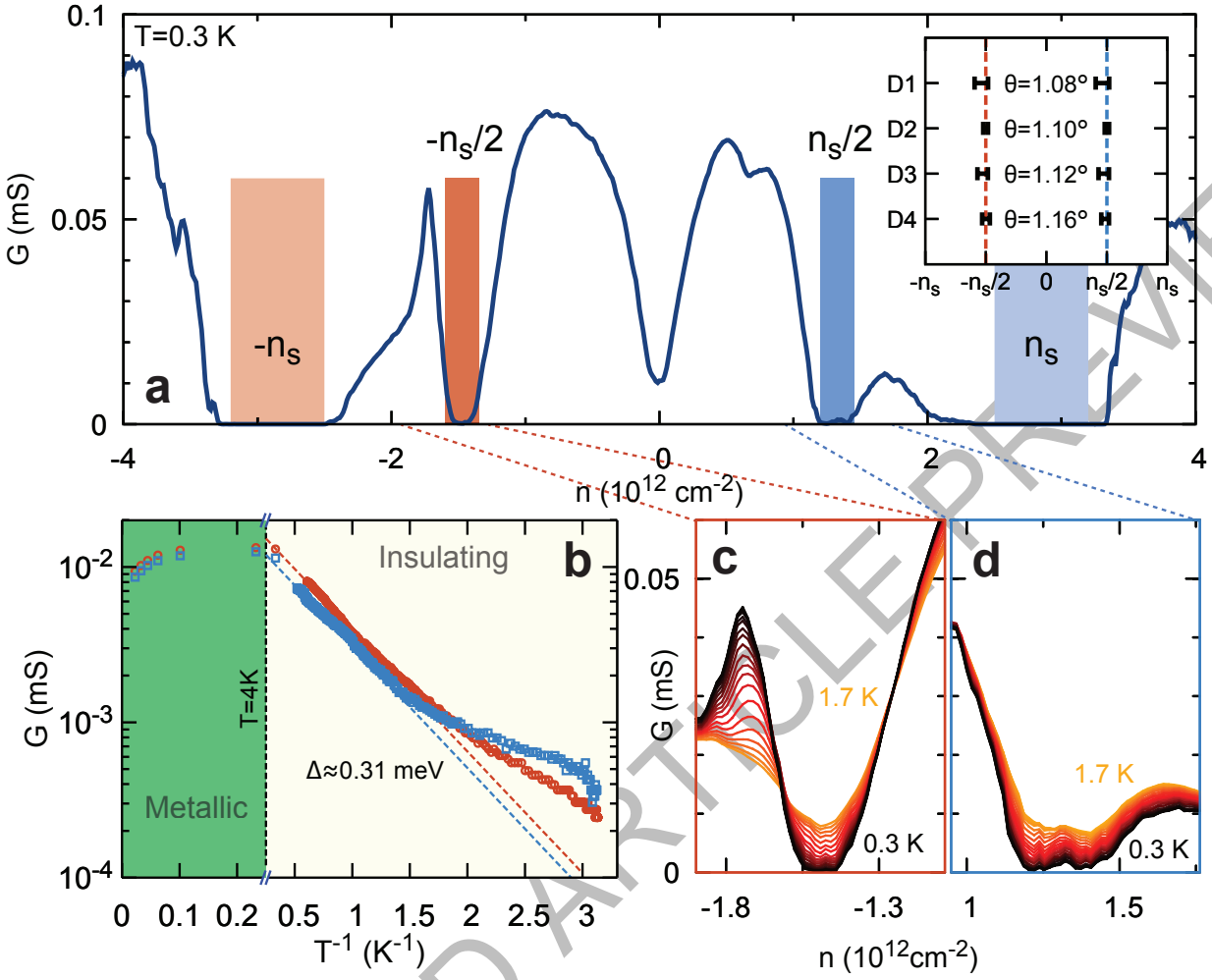

Figure 2 | Half-filling insulating states in magic-angle TBG (MA-TBG). (a) Measured conductance of a MA-TBG device D1 with $\theta = 1.08°$. Dirac point is located at $n = 0$. The lighter shaded regions are superlattice gaps at carrier density $n = \pm n_s = \pm 2.7 \times 10^{12}\,\mathrm{cm}^{-2}$. The darker shaded regions denote half-filling states at $\pm n_s/2$. Inset shows the density locations of half-filling states in four different devices. Definition of the error bars is explained in the Methods. (b) Minimum conductance values in the p-side and n-side half-filling states in device D1, labeled by corresponding colors as defined in (a) and (c-d). The dashed lines are fits of the formula $\exp[-\Delta/(2kT)]$ to the data, where $\Delta \approx 0.31$ meV is the thermal activation gap. (c-d) Temperature dependent conductance of D1 from about 0.3–1.7 K near the (c) p-side and (d) n-side half-filling states.

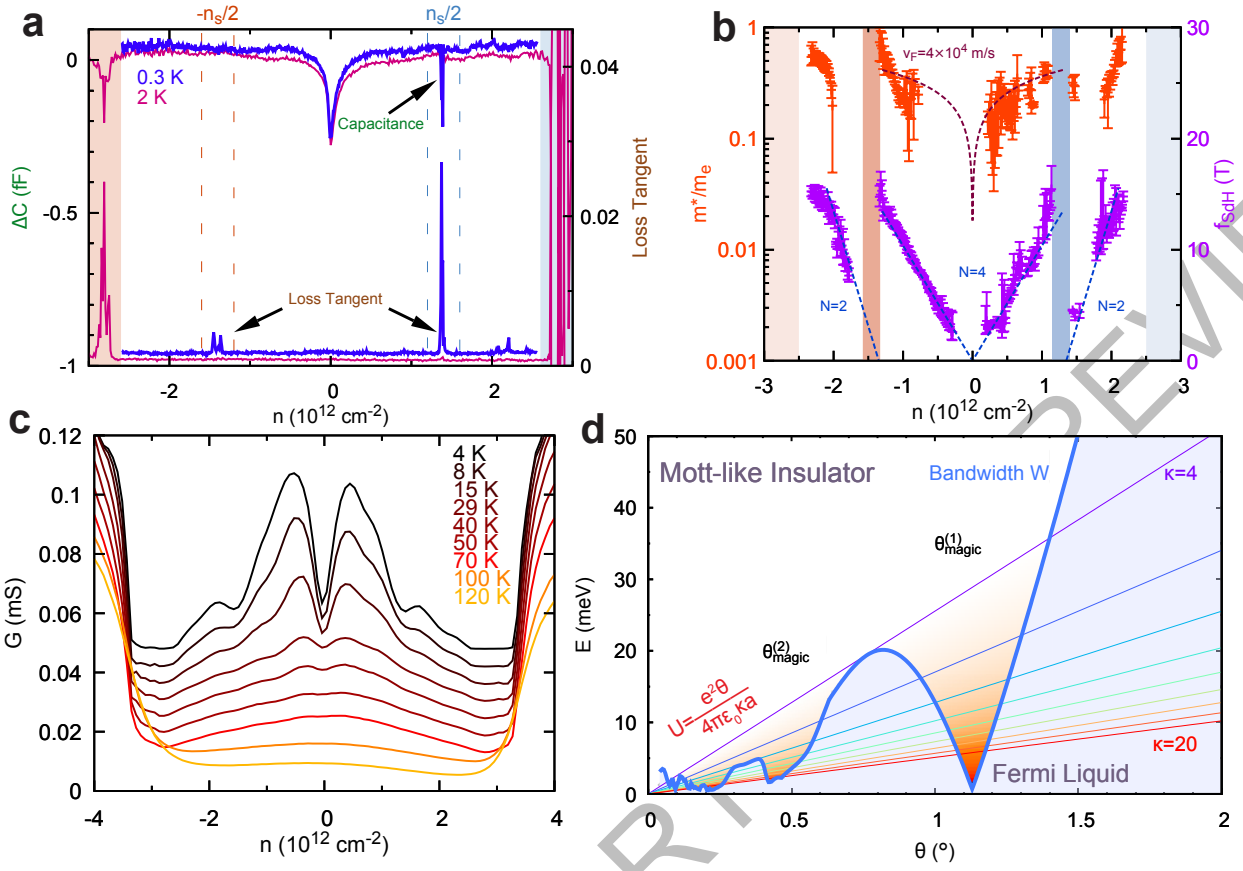

Figure 3 | Flat bands in MA-TBG. (a) Capacitance measurements of device D2 at 0.3 K (blue trace) and 2 K (pink trace). The change in the measured capacitance (upper traces), ΔC, is plotted on the left axis, and the loss tangent (lower traces) is shown on the right axis. For density corresponding to half-filling $\pm n_s/2$, reduction in ΔC (on p-side only) and enhancement in loss tangent (on both sides) are observed (0.3 K data). These effects disappear in the 2 K measurements. (b) The effective mass m^* and oscillation frequency f_{SdH} as extracted from temperature-dependent SdH oscillations. The fitting curves are $m^* = \sqrt{h^2 n/(8\pi v_F^2)}$, assuming a uniform Fermi velocity v_F. For magic-angle device D1 the estimated Fermi velocity $v_F = 4 \times 10^4$ m s^{-1} is 25-times reduced from that in pristine graphene, $v_0 = 1 \times 10^6$ m s^{-1}. The measured oscillation frequencies point towards the existence of small Fermi pockets that start from the half-filling states with one half the degeneracy of the main Fermi surface of the Dirac points. Shaded regions at half-filling and full-filling correspond to the shaded rectangles in Fig. 2a. (c) Gate-dependence of the conductance of D1 at different temperatures from 4.5 K to 120 K. The curves are vertically shifted by 0.006 mS between each curve for clarity. See Extended Data Fig. 5a, b for a full temperature dependence up to room temperature. (d) The comparison between the bandwidth W for the $E > 0$ flat band branch in TBG and the on-site energy U for different twist angles. Near the magic angles $\theta^{(i)}_{magic} \approx 1.1°, 0.5°, \ldots, U > W$ is satisfied for a range of possible κ (defined in the main text), and the system can be driven into a Mott-like insulator.

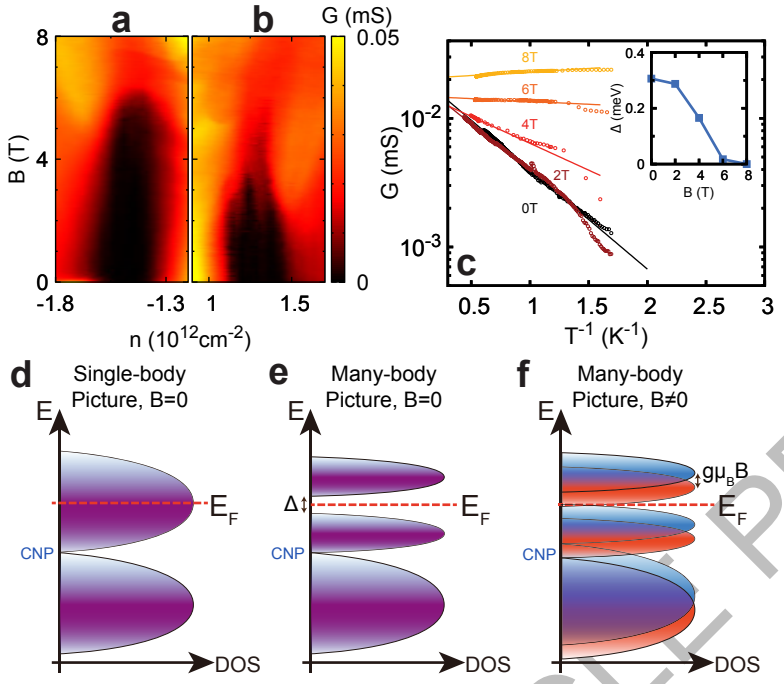

Figure 4 | Magnetic field response of the half-filling insulating phases. (a-b) $B_\perp$ dependence of the conductance of the half-filling states for D1 on (a) p-side and (b) n-side. The measurement is taken at 0.3 K. (c) Arrhenius plot of the conductance of the p-side half-filling state at different magnetic fields. The inset shows the thermal activation gap extracted from fitting the data of the main plot with $\exp[-\Delta/(2kT)]$. (d-f) Schematic density of states (DOS) pictures. The single-particle flat-bands (both $E>0$ and $E<0$ bands are shown, with E_F in the $E>0$ band, i.e. n-doping) in (d) is split into upper and lower many-body bands by interactions (e). This occurs when E_F is at half-filling of the upper band. Upon applying a Zeeman field, the excitations can be further polarized and close the charge gap when the Zeeman energy is comparable to the gap (f). Purple shading denotes a spin-degenerate band, while blue and red shading denote spin-up and spin-down bands respectively. CNP abbreviates for charge neutrality point. The shape of the DOS drawn here is purely illustrative and does not represent the actual DOS profile (see Extended Data Fig. 6 for numerical result).

METHODS

Sample preparation. Device D1, D2 and D4 are fabricated using a modified 'tear & stack' technique detailed in previous works.[13,17,22] Monolayer graphene and hexagonal boron nitride (h-BN, 10 to 30 nm thick) are exfoliated on SiO_2/Si chips and examined with optical microscopy and atomic force microscopy. We use a Poly(Bisphenol A carbonate) (PC)/Polydimethylsiloxane (PDMS) stack on a glass slide mounted on a micro-positioning stage to first pick up h-BN flake at 90 °C. Then we use the van der Waals force between h-BN and graphene to tear a graphene flake at room temperature. The separated graphene pieces are manually rotated by an angle θ about 0.2°–0.3° larger than the desired twist angle and stacked together again, resulting in a precisely controlled TBG structure. The TBG is then encapsulated by picking up another h-BN flake on the bottom, and the entire stack released onto a metal gate at 160 °C. The final device geometry is defined by electron-beam lithography and reactive ion etching. Device D3 is fabricated using a slightly different procedure, where independent graphene flakes are stacked together. The edges of graphene flakes are aligned under optical microscope to obtain small twist angles.

Measurements. Transport measurements are performed using a standard low frequency lock-in amplifier with excitation frequency of about 10–20 Hz and excitation voltage of 100 μV, in a He-3 cryostat. The current flowing through the device is amplified by a current pre-amplifier and then measured by the lock-in amplifier.

Capacitance was measured using a low-temperature balanced capacitance bridge.[23] A schematic of the measurement circuit is shown in Extended Data Fig. 2a. The reference capacitance C_{ref} used in our experiment is approximately 40 fF, and the device geometrical capacitance is approximately 7 fF. The ac excitation voltage used in our measurements is 3 mV at $f = 150$ kHz.

Transport data in device D4. Transport measurements in both D1 and D3 were performed in a two-probe configuration. Although it is generally advised to perform four-probe measurements in transport experiments, we find that the existence of multiple insulating states (both the superlattice gaps at $\pm n_s$ and half-filling states at $\pm n_s/2$) frequently lead to noisy or negative R_{xx} signals due to the region in the device near the voltage probes becoming insulating at a slightly different carrier density. In our case where we are mostly interested in the insulating behaviours on the order of 100 kΩ to 1 MΩ, a contact resistance of at most a few kΩ that is typical in edge-contacted graphene device does not obscure the present data.[33] Thus we believe that the two-probe data presented throughout the paper is fully trustable and gives an accurate presentation of the device characteristics.

Extended Data Fig. 4b, c show the measurements of the two-probe and four-probe conductances in a fourth device D4, which has a twist angle of $\theta = 1.16° \pm 0.02°$. Device D4 was measured in a Hall-bar configuration so that the contact resistance can be removed. In this particular device, both the superlattice insulating states and the half-filling states do not have very high impedance (probably due to disorder and/or inhomogeneity), and therefore the previously described issues with four-probe measurements did not occur. It is clear that the four-probe and two-probe measurements essentially show the same features, while some weak signals appear to be better resolved in the four-probe measurements.

In the four-probe data, we not only observe the half-filling states (±2 electrons per moiré unit cell), we also see evidence for odd-filling insulating phases at ±3 electrons per moiré unit cell as weak reduction in the conductance curve. Note that the existence of insulating behaviours at other integer fillings of the flat bands than ±2 is a result to be expected in the Mott-like insulator picture, and further lends support to our claim that the correlated insulating behaviour originates from the on-site Coulomb interaction.

Hall measurement in device S4. We have also measured the device D4 in a Hall configuration (R_{xy}). Extended Data Fig. 4d, e show the low-field linear Hall coefficient $R_H = R_{xy}/B$ and the Hall density $n_H = -1/(eR_H)$ versus gate-induced charge density n. In a uniformly gated single-carrier two-dimensional electronic gas, one expects that $n_H = n$. This is what we have measured in the density range $(-1.3–1.3) \times 10^{12}$ cm^{-2} at 0.3 K. Near the half-filling states $n = \pm n_s/2$, however, the Hall density abruptly jumps from $n_H = n$ to a small value close to zero (but not changing its sign). Beyond half-filling, n_H follows $n_H = n \pm n_s/2$, a new trend that is consistent with quasiparticles that are generated from the half-filling states. This 'resetting' effect of the Hall density gradually disappears as the temperature is raised from 0.3 K to 10 K, in agreement with the energy scale of the Mott-like states. At higher temperatures, the Hall density is linear with n but the slope is no longer one, which might be related to the thermal energy kT being close to the bandwidth, resulting in thermally excited carriers with opposite polarity reducing the net Hall effect.

We note that in good correspondence with the quantum oscillation data shown in Fig. 3b, we only see the behaviors of the new quasiparticles on one side of the Mott-like state, e.g. the side further from the charge neutrality point; between the charge neutrality point and the Mott-like state, we see an abrupt change from the typical large Fermi surface of the single-particle bands to a small Fermi surface of the new quasiparticles. This may result if the effective mass of the quasiparticles on one side of the Mott-like gap is considerably greater than the other side, so that the oscillation and Hall effect become difficult to observe very close to the metal-insulator transition.

Determination of the twist angle. Accurate determination of the twist angles of the samples is of utmost importance in understanding the magic-angle physics. We use several independent methods to determine the twist angle from transport data.

1. The superlattice density n_s, defined by the density required to fill one band in the superlattice, is related to the twist angle by

$$n_s = \frac{4}{A} \approx \frac{8\theta^2}{\sqrt{3}a^2} \quad (1)$$

where A is the unit cell area, $a = 0.246$ nm is the lattice constant of graphene. At approximately $1° < \theta < 3°$, the superlattice densities $\pm n_s$ are associated with a pair of single-particle bandgaps at their corresponding Fermi energy.[13,34,35] Therefore, the measured density of the superlattice insulating states can be used to directly estimate θ according to Eq. (1). Due to localized states, the accurate value of n_s is difficult to pinpoint at zero magnetic field, and the estimated θ has an uncertainty of about 0.1°–0.2°. Extended Data Fig. 7a-d shows the resistivity (resistance for magic-angle device D1) for four different TBG samples of twist angles $\theta = 1.38, 1.08, 0.75, 0.65°$ respectively. At $\theta \sim 1.38, 1.08°$, the positions of the superlattice gaps clearly provide an good estimation of θ. However, it is noted in Ref. 17 that the apparent resistance peaks in the transport data may not correspond to n_s but instead $2n_s$, when the twist angle is below 0.9∼1°. We have observed a similar phenomenon when twist angle is as small as 0.65°. This complicates the determination of twist angles, since one encounters an ambiguity of whether the feature one observes corresponds to n_s or $2n_s$, which can result in the twist angle wrong by a factor of $\sqrt{2}$.

2. We use the fact that each band edge of the mini-band structure has its own Landau levels.[13,34,36] Extended Data Fig. 7e shows the magneto-conductance data of device D1 (taken first derivative with respect to n). The Landau levels emanating from $n_s = (2.7 \pm 0.1) \times 10^{12}$ cm^{-2} can be clearly seen, which translates to $\theta = 1.08° \pm 0.02°$ according to Eq. (1). Since the intersection points of the Landau levels can be determined relatively accurately (uncertainty of about 1×10^{11} cm^{-2}), the twist angle can be determined with an uncertainty of about 0.02° near the first magic angle.

3. The effect of applying strong magnetic fields such that the magnetic length becomes comparable with the unit cell size is described by Hofstadter's butterfly model.[37] In density space, this model is better captured in Wannier's picture.[38] In the Wannier diagram, the Landau levels are universally represented by $n/n_s = \nu\phi/\phi_0 + s$, where ϕ is the magnetic flux through a unit cell and ν is an integer. $s = 0$ labels the main Landau fan and $s = \pm 1$ is the (first) satellite fan, etc. Adjacent Landau fans intersect when $\phi/\phi_0 = 1/q$, or equivalently, $1/B = qA/\phi_0$, where q is another integer. Therefore, in the experiments one would expect to see Landau level crossings at periodic intervals of $1/B$, of which the periodicity is proportional to the unit cell area A. This effect has been observed in other two-dimensional superlattice systems, and can be utilized to cross-check the twist angles extracted from other methods.[2–4] Extended Data Fig. 7f shows the magneto-transport data (first derivative with respect to density) of device D3 at high doping densities, plotted versus n and $1/B$. A periodic crossing of Landau levels is clearly observed near at -9×10^{12} cm^{-2}. The periodicity is 0.033 ± 0.001 T^{-1}, which gives $A = (1.37 \pm 0.04) \times 10^{-12}$ cm^2 and $\theta = 1.12° \pm 0.01°$, compared to $\theta = 1.12° \pm 0.02°$ extracted using the previous method ($n_s = (2.9 \pm 0.1) \times 10^{12}$ cm^{-2}).

Estimation of the Fermi velocity from capacitance data. The measured capacitance is the series sum of geometric capacitance C_{geom} and quantum capacitance C_q. The latter is directly proportional to the density of states (DOS) in TBG. Therefore, by analyzing the quantum capacitance C_q as a function of carrier density n, one can extract the dependence of DOS on n, and subsequently deduce the Fermi velocity.

In the zero temperature limit, the quantum capacitance is related to the DOS by $C_q = e^2 D(E_F)$, where E_F is the Fermi energy. A model system for TBG near the charge neutrality consists of massless Dirac fermions with Fermi velocity v_F and 8-fold degeneracy (spin, valley, layer), the DOS is[39–41]

$$D(E_F) = \frac{4}{\pi} E_F (\hbar v_F)^2$$

Since $E_F = \hbar v_F k_F$ is related to the density n by

$$n = 8\frac{1}{(2\pi)^2}\pi k_F^2 = \frac{2}{\pi}\frac{E_F^2}{(\hbar v_F)^2}$$

$$E_F = \hbar v_F \sqrt{\frac{n\pi}{2}}$$

where the factor of 8 comes from spin, valley, and layer, the quantum capacitance of the TBG is therefore written as

$$C_q = e^2 \frac{2\sqrt{2}}{\sqrt{\pi}\hbar v_F} \sqrt{|n| + n_d} \quad (2)$$

Due to disorder, the spatially averaged DOS at the Dirac point ($n = E_F = 0$) will not be absolutely zero. Therefore a phenomenological $n_d \approx 1 \times 10^{10}\,\mathrm{cm}^{-2}$ is added in the expression above.[39]

The measured capacitance is then

$$\frac{1}{C} = \frac{1}{C_{geom}} + \frac{1}{C_q} \quad (3)$$

In Extended Data Fig. 2b, we show the measured capacitance near the Dirac point and fitting curves according to Eq. (2) and Eq. (3). The C_{geom} is approximated by the DC gating capacitance $C_g \approx 7.5$ fF. We find that using parameters $v_F = 0.15 \times 10^6\,\mathrm{m\,s}^{-1}$ and $n_d = 1 \times 10^{10}\,\mathrm{cm}^{-2}$ gives a reasonable fit to the data measured at both 0.3 K and 2 K.

We note that the fitting for v_F is sensitive to the value used for C_{geom}. For example, using a C_{geom} value 30% larger than the value we used above, we find a Fermi velocity of $v_F = 0.10 \times 10^6\,\mathrm{m\,s}^{-1}$. Similarly, using a value 15% smaller than the said value we find $v_F = 0.20 \times 10^6\,\mathrm{m\,s}^{-1}$. Nonetheless, the analysis present here suffices to demonstrate that the Fermi velocity is indeed greatly reduced in the capacitance device D2. The slightly larger Fermi velocity compared to that measured in the transport device D1 $v_F = 0.04 \times 10^6\,\mathrm{m\,s}^{-1}$ can be attributed to the slightly larger twist angle of device D2 $\theta = 1.10°$, which might be further from the first magic angle $\theta^{(1)}_{magic} \approx 1.05°$.

Error bar in Fig. 2a inset. The error bars in Fig. 2a are computed using the following criteria:

• For the transport devices D1, D3 and D4, the endpoints of the error bars correspond to the points where the conductance rises to 10% of the peak value on that side.

• For the capacitance device D2, since the peaks are very sharp (see Fig. 3a), the error bar corresponds to the width of the entire peaks in the loss tangent data.

Quantum Oscillations and Extraction of m^*. We performed magnetotransport measurements in device D1 from 0.3 K to 10 K. At each gate voltage, a polynomial background of resistance in B is first removed, and then the oscillation frequency and the effective mass is analysed. Examples of the SdH oscillations and their temperature dependences at a few representative gate voltages are shown in Extended Data Fig. 3a-c. Temperature dependence of the most prominent peak is fitted with the Lifshitz–Kosevich formula applied to conductance

$$\Delta R \propto \frac{\chi}{\sinh(\chi)}, \quad \chi = \frac{2\pi^2 kT m^*}{\hbar e B} \quad (4)$$

and the cyclotron mass m^* is extracted from the fitting (examples shown in Extended Data Fig. 3d). Within the flat bands, the quantum oscillations universally disappear at around 10 K except very close to the Dirac point, again consistent with the large electron mass and greatly reduced Fermi velocity near the first magic angle.

The full magnetoconductance map measured in device D1 at 0.3 K is shown in Extended Data Fig. 5c. At a first glance, it may seem that the Landau levels emanating from the Dirac point 'penetrate' the half-filling states and continue towards the band edges. However, upon closer examination this is not the case. Extended Data Fig. 3e-f shows the same data but plotted versus $1/B$ instead of B. Here it can be seen that at densities beyond the half-filling states, the oscillations are clearly not converging at the Dirac point, but instead at the half-filling states themselves. The oscillation frequencies extracted from this data are plotted in Fig. 3b.

Discussion of the band structure of TBG near magic angles. The general evolution of the band structure of TBG above the first magic angle is described in a number of earlier works.[6,14–16,18,34,35] The low-energy band structure consists of two Dirac cones (each is 4-fold degenerate due to valley and spin), with a renormalized Fermi velocity

$$v_F(\theta) = \frac{1 - 3\alpha^2}{1 + 6\alpha^2} \approx 1 - 9\alpha^2 \quad (\alpha \le 1)$$

where $\alpha = w/(v_0 k_\theta)$ is the dimensionless interlayer hopping amplitude (w, v_0 are the interlayer hopping energy and original Fermi velocity in graphene, $k_\theta \approx K\theta$ is the interlayer momentum difference, K is the wave number at the corner of graphene's Brillouin zone).[6,15] $v_F(\theta)$ passes through zero at $\alpha = 1/\sqrt{3}$, which defines the first magic angle $\theta^{(1)}_{magic}$. However, to the best of our knowledge the detailed evolution of the band structure near the magic angles has not been addressed in the literature. Specifically, we ask the following question: as the Fermi velocity at the Dirac points changes sign, how does the associated *winding number* evolve? Close to a generic Dirac point, the effective two-band Hamiltonian can be written as[42]

$$\mathcal{H}(\boldsymbol{k}) = v_F(\theta)\boldsymbol{\sigma}\cdot\boldsymbol{k} + \mathcal{O}(k^2) = \begin{bmatrix} \mathcal{O}(k^2) & v_F(\theta)\boldsymbol{k}^\dagger + \mathcal{O}(k^2) \\ v_F(\theta)\boldsymbol{k} + \mathcal{O}(k^2) & \mathcal{O}(k^2) \end{bmatrix}$$

in which $\boldsymbol{k} = k_x + ik_y$. When $v_F(\theta) \to 0$ near the first magic angle, the terms linear in k vanish and the dispersion is dominated by the next-leading-order k^2 terms. A simple form of the k^2 term is

$$\mathcal{H}(\boldsymbol{k}) = \begin{bmatrix} 0 & v_F(\theta)\boldsymbol{k}^\dagger + \frac{1}{2m}\boldsymbol{k}^2 \\ v_F(\theta)\boldsymbol{k} + \frac{1}{2m}(\boldsymbol{k}^\dagger)^2 & 0 \end{bmatrix} \quad (5)$$

in which m is a parameter with the dimension of mass. In fact, this Hamiltonian describes the low-energy band dispersion of monolayer graphene with third-nearest-neighbour hopping, as well as bilayer graphene with Bernal stacking and trigonal warping.[42–46] The eigenvalues of this Hamiltonian are

$$E_\pm(\boldsymbol{k}) = \pm\sqrt{\left[v_F k_x + \frac{1}{2m}(k_x^2 - k_y^2)\right]^2 + \left[v_F k_y - \frac{1}{m}k_x k_y\right]^2} \quad (6)$$

The evolution of the dispersion described by Eq. (6) with varying v_F and a constant $m = 0.5$ is shown in Extended Data Fig. 1a–f. The winding number associated with a Dirac point is defined by

$$w = \frac{i}{2\pi}\oint_C \boldsymbol{k}|\nabla_{\boldsymbol{k}}|\boldsymbol{k}\cdot d\boldsymbol{k}$$

where C is a loop around that Dirac point. The winding number follows a conservation law when the motion and merging of Dirac points are considered.[42] The winding number of each band touching point is labelled in Extended Data Fig. 1a–f.

When $v_F \to 0$ there exist three additional Dirac points with opposite winding numbers (-1) to the main Dirac point ($+1$). Therefore at $v_F = 0$ when all four Dirac points merge, the winding number is -2, since the total winding number cannot change.

The simple Hamiltonian form of Eq. (5) is an educated guess. We performed numerical calculations of the winding number using the continuum model for TBG[6,15] and the numerical method in Ref. 47. The results are summarized in Extended Data Fig. 1g-l. We find that near the first magic angle of the model being used, $\theta^{(1)}_{magic} = 1.064°$, the picture described in Extended Data Fig. 1a-f is exactly what happens at each corner of the mini Brillouin zone (MBZ). The complication that arises when one considers the entire MBZ is that, for a given valley (of the original grapheme Brillouin zone, *e.g. K*), the two inequivalent corners of the MBZ have the *same* winding number, because they are the hybridized result of the same valley (K) of opposite *layers* (see Fig. 1d of the main text). Global time reversal symmetry is preserved by mapping to the other valley (K'). Therefore, for a given valley K, when the twist angle is reduced from large angles where the winding numbers of the two corners are (+1, +1) to the first magic angle where the winding numbers are (-2,-2), a net winding number change $\Delta w = 6$ occurs between the two lowest energy bands. Further theoretical work is necessary to elucidate the physics behind this winding number evolution near the first magic angle.

In summary, we show that at *exactly* the first magic angle, the Dirac point at each corner of the MBZ (K_s and K_s') becomes a parabolic band touching with winding number -2, similar to bilayer graphene with Bernal stacking except that the two corners have the same winding number. The calculation corresponding to the first magic angle in Extended Data Fig. 1i can be fit to a paraboloid, giving an effective mass of $1.1 m_e$. This value can be viewed as the asymptotic limit of the effective mass near the charge neutrality point as $v_F \to 0$.

Density of states (DOS) in MA-BLG. Despite our simplistic representation of the DOS in the flat-bands of MA-TBG in main Fig. 4d-f, the actual single-particle DOS profile of MA-TBG is rather complex with multiple van Hove singularities (vHs). In Extended Data Fig. 6 we show a DOS versus energy plot calculated with the continuum model as presented in Ref. 6 for $\theta = 1.08°$.

Data availability. The data that support the findings of this study are available from the corresponding author on reasonable request.

33. Wang, L. *et al.*, One-Dimensional Electrical Contact to a Two-Dimensional Material. *Science* **342**, 614–617 (2013).
34. Moon, P. & Koshino, M., Energy spectrum and quantum Hall effect in twisted bilayer graphene. *Phys. Rev. B* **85**, 195458 (2012).

35. Nam, N. N. T. & Koshino, M., Lattice relaxation and energy band modulation in twisted bilayer graphenes. *Phys. Rev. B* **96**, 075311 (2017).
36. Kim, Y., *et al*., Charge Inversion and Topological Phase Transition at a Twist Angle Induced van Hove Singularity of Bilayer Graphene. *Nano Lett.* **16**(8), 5053–5059 (2016).
37. Hofstadter, D. R., Energy levels and wave functions of Bloch electrons in rational and irrational magnetic fields. *Phys. Rev. B* **14**, 2239 (1976).
38. Wannier, G. H. & A Result Not Dependent on Rationality for Bloch Electrons in a Magnetic Field. *physica status solidi (b)* **88**, 757–765 (1978).
39. Xia, J., Chen, F., Li, J. & Tao, N., Measurement of the quantum capacitance of graphene. *Nat. Nanotech*. **4**, 505–509 (2009).
40. Fang, T., Aniruddha, K., Xing, H. & Jena, D., Carrier statistics and quantum capacitance of graphene sheets and ribbons. *App. Phys. Lett.* **91**, 092109 (2007).
41. Wallace, P. R., The Band Theory of Graphite. *Phys. Rev*. **71**, 622 (1947).
42. Goerbig, M. & Montambaux, G., Dirac Fermions in condensed matter and beyond. arXiv:1410.4098 (2014).
43. Bena, C. & Simon, L., Dirac point metamorphosis from third-neighbor couplings in graphene and related materials. *Phys. Rev. B* **83**, 115404 (2011).
44. Montambaux, G., An equivalence between monolayer and bilayer honeycomb lattices. *Eur. Phys. J. B* **85**, 375 (2012).
45. McCann, E. & Koshino, M., The electronic properties of bilayer graphene. *Rep. Prog. Phys.* **76**, 056503 (2013).
46. McCann, E. & Fal'ko, V. I., Landau-Level Degeneracy and Quantum Hall Effect in a Graphite Bilayer. *Phys. Rev. Lett*. **96**, 086805 (2006).
47. Fukui, T., Hatsugi, Y. & Suzuki, H., Chern Numbers in Discretized Brillouin Zone: Efficient Method of Computing (Spin) Hall Conductances. *J. Phys. Soc. Jpn.* **74**, 1674–1677 (2005).

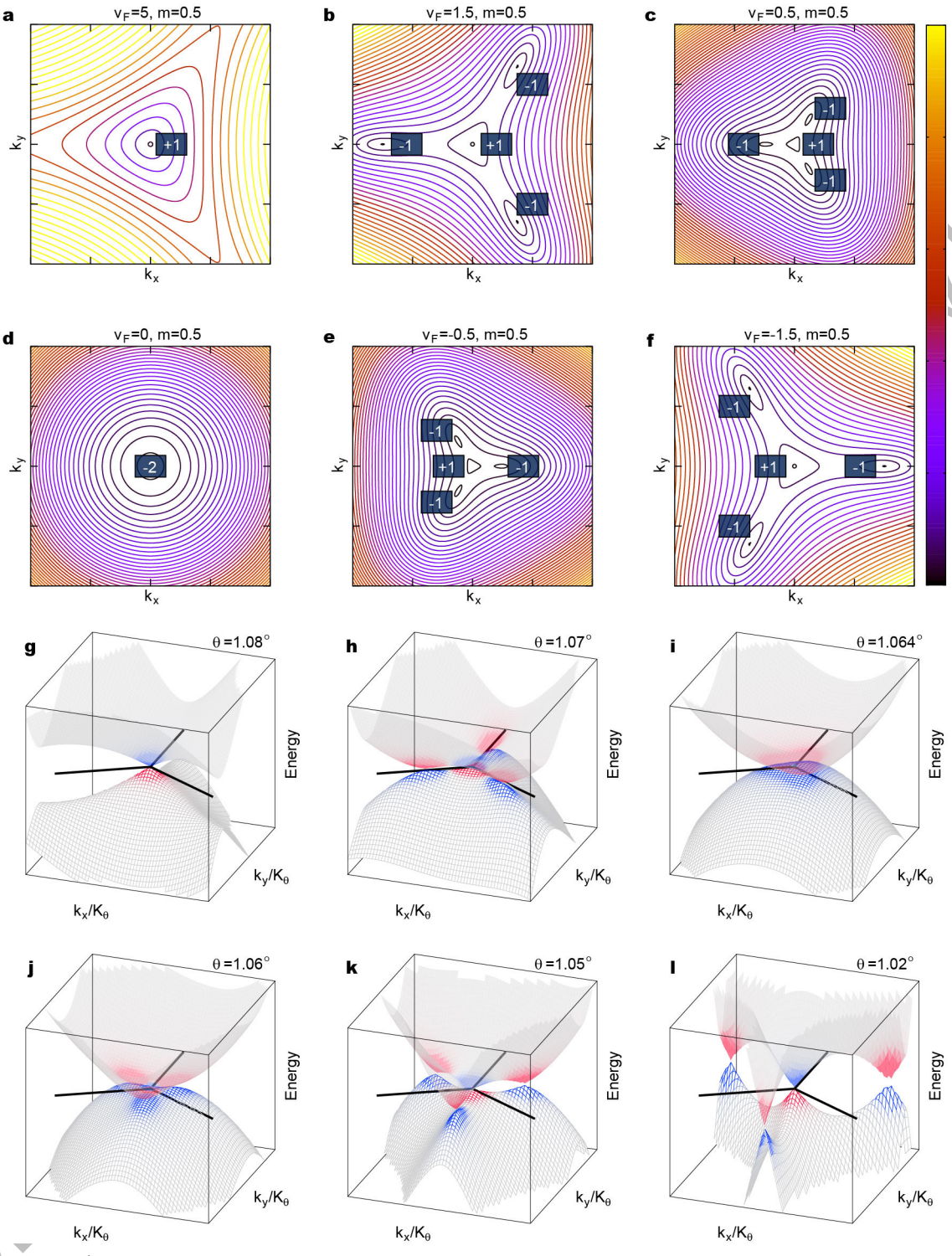

Extended Data Figure 1 | Evolution of low-energy band structure of TBG near the magic angle. (a-f) E_+ dispersion as in Eq. (6) for different v_F and fixed $m = 0.5$. The k_x and k_y range in the figures is $[-2, 2]$, while the scale of the colorbar (on the right side of the figures) for the energy axis is [0, 10] from bottom to top. The associated winding number of each band touching point is labeled in the figures. (g-l) The evolution of the low-energy band structure of TBG near the first magic angle $\theta^{(1)}_{\text{magic}} = 1.064°$ in the model. The color shows the hotspots of the Berry curvature at each band touching point. Note that the energy axis spans an extremely small range of [-50, 50] μeV. The momentum axes are measured by $k_\theta \approx K\theta$ and the range for both k_x/K_θ and k_y/K_θ is [-0.1, 0.1]. The center of the momentum space is the K_s point of the MBZ (see main Fig. 1d), and the thick lines denotes the K_s–M_s–K_s' directions (there are three inequivalent ones). All results are shown for the K-valley continuum description of TBG.[6]

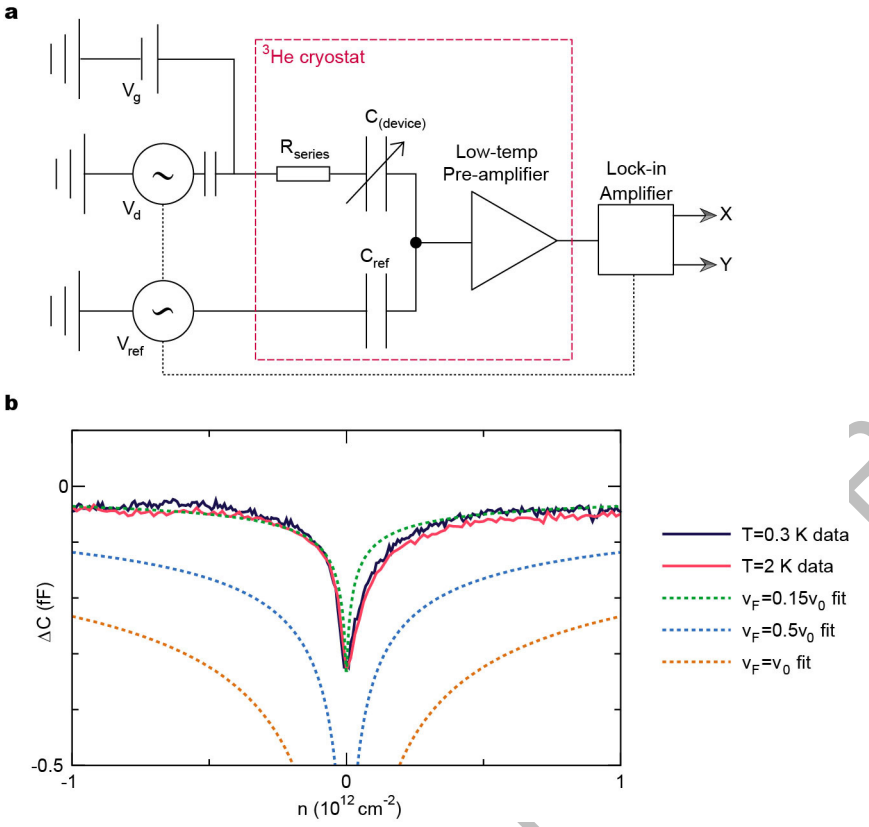

Extended Data Figure 2 | Capacitance measurement setup and extraction of the Fermi velocity. (a) Schematic for the low-temperature capacitance bridge. The X and Y outputs from the lock-in amplifier refer to the in-phase and out-of-phase components respectively. $C_{(device)}$ and R_{series} are the capacitance and resistance of the sample. V_g is the DC gate voltage. All connections into and out from the cryostat are made with coaxial cables. (b) Capacitance of device D2 near the charge neutrality point, and fitting curves according to Eq. (4, 5) with different Fermi velocities. $v_0 = 10^6$ m s^{-1} is the Fermi velocity in pristine graphene.

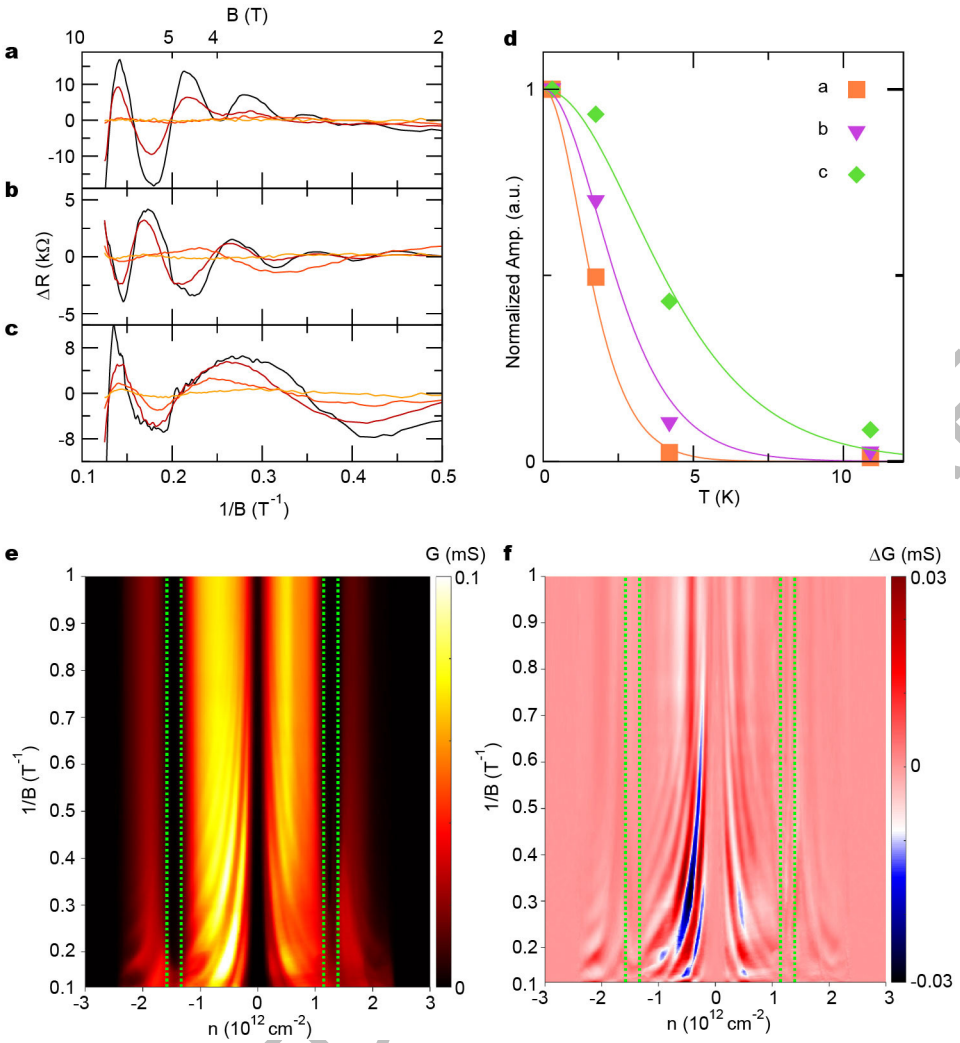

Extended Data Figure 3 | Quantum oscillations and extraction of the effective mass. (a-c) Temperature-dependent magnetoconductance of device D1 at gate voltages (a) $n = -2.08 \times 10^{12}\,\mathrm{cm}^{-2}$, (b) $n = -1.00 \times 10^{12}\,\mathrm{cm}^{-2}$ and (c) $n = 0.19 \times 10^{12}\,\mathrm{cm}^{-2}$. The temperatures are from dark to bright, 0.3 K, 1.7 K, 4.2 K and 10.7 K respectively. The figure on the right summarizes the oscillation amplitudes of the most prominent peaks in (a-c). The curves are fitted according to the L-K formula Eq. (4). (e) Magnetoconductance of device D1 (measured at 0.3 K) plotted versus n and $1/B$. (f) The same data with a polynomial background in B removed for each density. The green boxes denote the range of density for the half-filling states. It can be seen that at densities beyond the half-filling states the oscillations are clearly not converging at the Dirac point, but instead the half-filling states themselves.

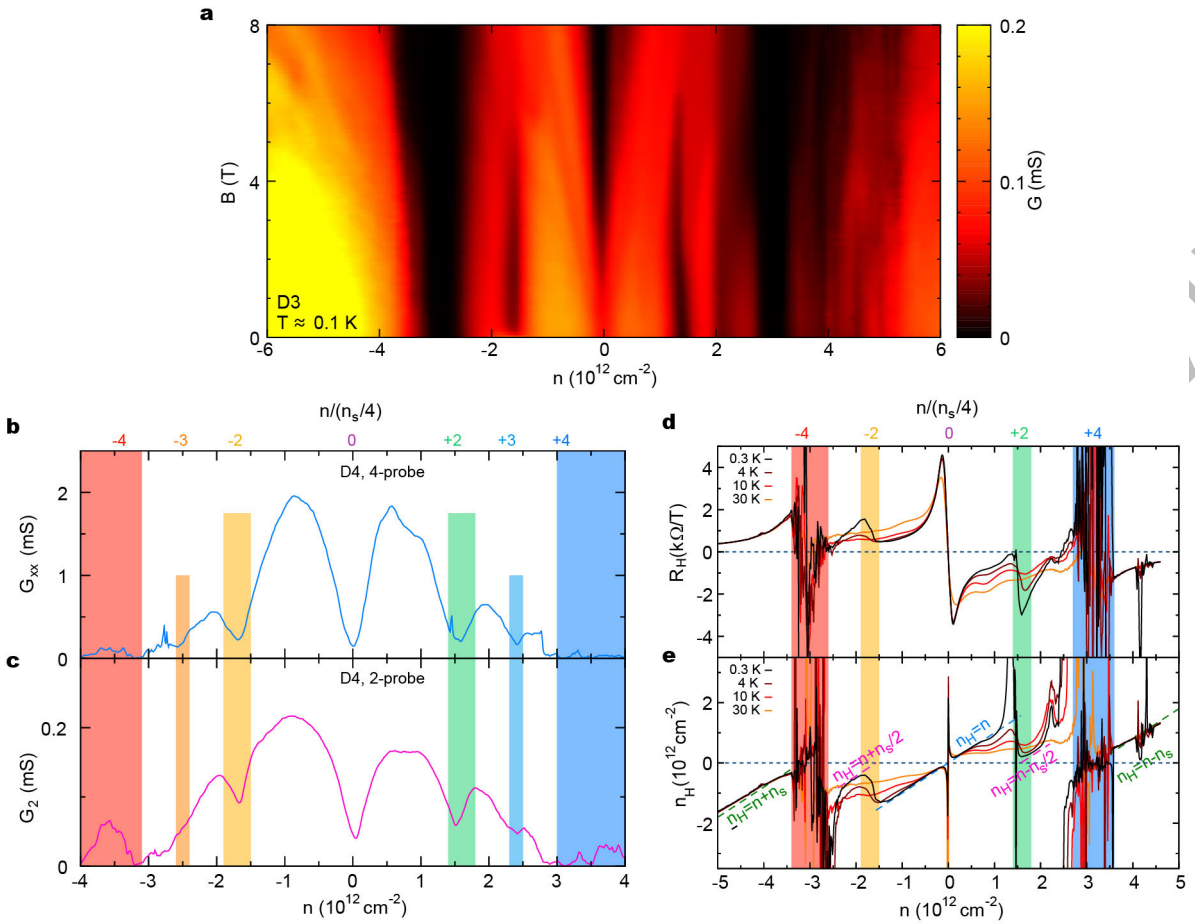

Extended Data Figure 4 | Supplementary transport data in device D3 and D4. (a) Magnetoconductance in device D3 ($\theta = 1.12°$) versus n and B. The primary features at the superlattice gaps $\pm n_s$ and the half-filling states $\pm n_s/2$ are essentially identical to device D1. (b-c) Four-probe and two-probe conductance measured in device D4 ($\theta = 1.16°$) at 0.3 K. The colored vertical bars and the corresponding numbers indicate the associated integer filling inside each unit cell of the moiré pattern. Besides clear observation of the half-filling states (± 2), we also observe weak drops in the four-probe conductivity that point towards three-quarter-filling states at ± 3. (d-e) Hall measurement in device D4 at various temperatures. (d) shows the Hall coefficients R_H while (e) shows the Hall density $n_H = -1/(eR_H)$. The colored vertical bars and the corresponding numbers indicate the associated integer fillings in the moiré unit cell. The x-axis is the gate-induced total charge density n, while the Hall density n_H and its sign indicates the number density and characteristic (electron-like or hole-like) of the carriers being transported.

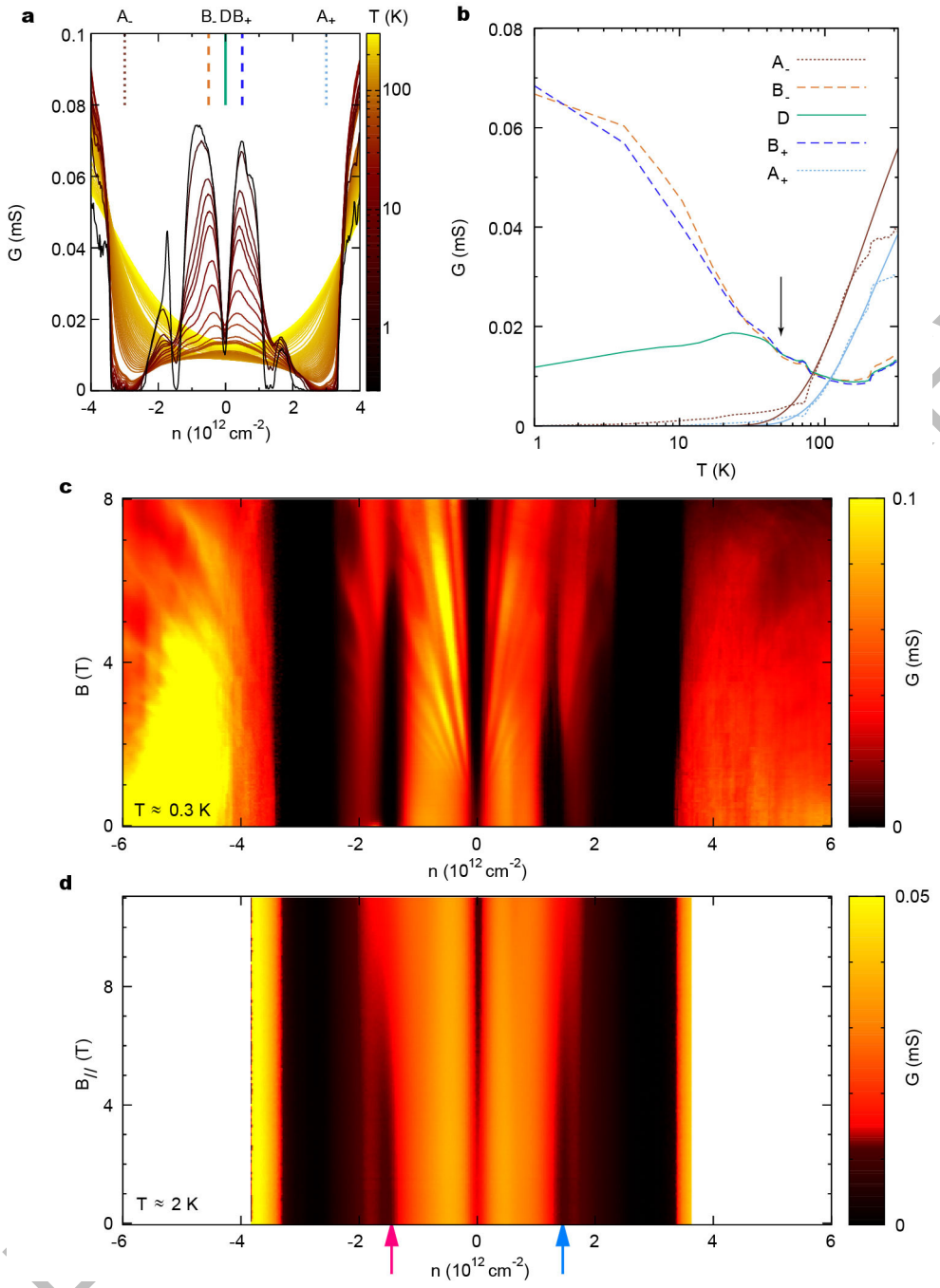

Extended Data Figure 5 | Supplementary transport data in device D1. (a) Temperature dependence of conductance of device D1 from 0.3 K to 300 K. (b) The conductance versus temperature at five characteristic carrier densities labelled $A_{\pm}$ (superlattice gaps), $B_{\pm}$ (above and below the Dirac point) and D (the Dirac point) in (a). The arrow denotes the temperature above which the conductances at $B_{\pm}$ merge with D. The solid lines accompanying $A_{\pm}$ traces are Arrhenius fit to the data. The thermal activation gaps of the superlattice insulating states at $A_{\pm}$ can be obtained by fitting the temperature dependence of the conductance at these densities. Detailed discussion about the superlattice gaps in non-magic-angle devices are published in Ref. 13. The fit to Arrhenius formula $\exp[-\Delta/(2kT)]$ yields $\Delta_{-} = 32$ meV for the A_{-} gap and $\Delta_{+} = 40$ meV for the A_{+} gap. For comparison, the same gaps measured in $\theta = 1.8°$ TBG are slightly larger at $\Delta_{-} = 50$ meV and $\Delta_{+} = 60$ meV for the gaps at negative and positive densities respectively.[13] (c) Magnetoconductance in device D1 as a function of gate-induced charge density n and perpendicular magnetic field B. (d) Magnetoconductance in device D1 measured as a function of n and *in-plane* magnetic field $B_{\parallel}$. The in-plane measurement is taken at a higher temperature of about 2 K. Combined with the degradation of the sample quality resulting from the thermal cycling that was necessary in order to change the field orientation, the half-filling states are not as well developed as in the previous measurements. However, the gradual suppression of the half-filling states is still unambiguously observed when $B_{\parallel}$ is above about 6 T, slightly higher but similar to the 4∼6 T threshold for the perpendicular field [see (c) and Fig. 4a, b].

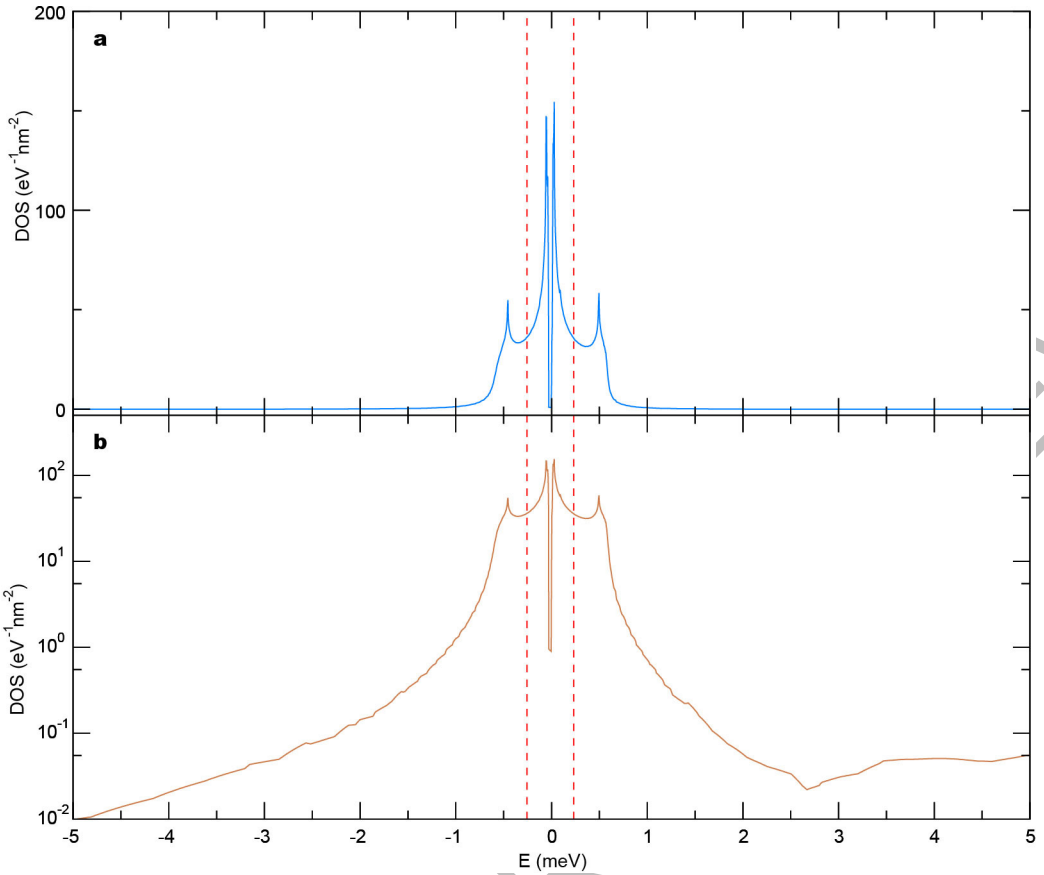

Extended Data Figure 6 | Density of states (DOS) in MA-TBG. Single-particle DOS in TBG at $\theta = 1.08°$, in linear (a) and logarithmic scale (b). The red dashed lines denotes the energy where the lower and upper flat bands are half-filled, respectively. The results are numerically obtained using the continuum model.[6]

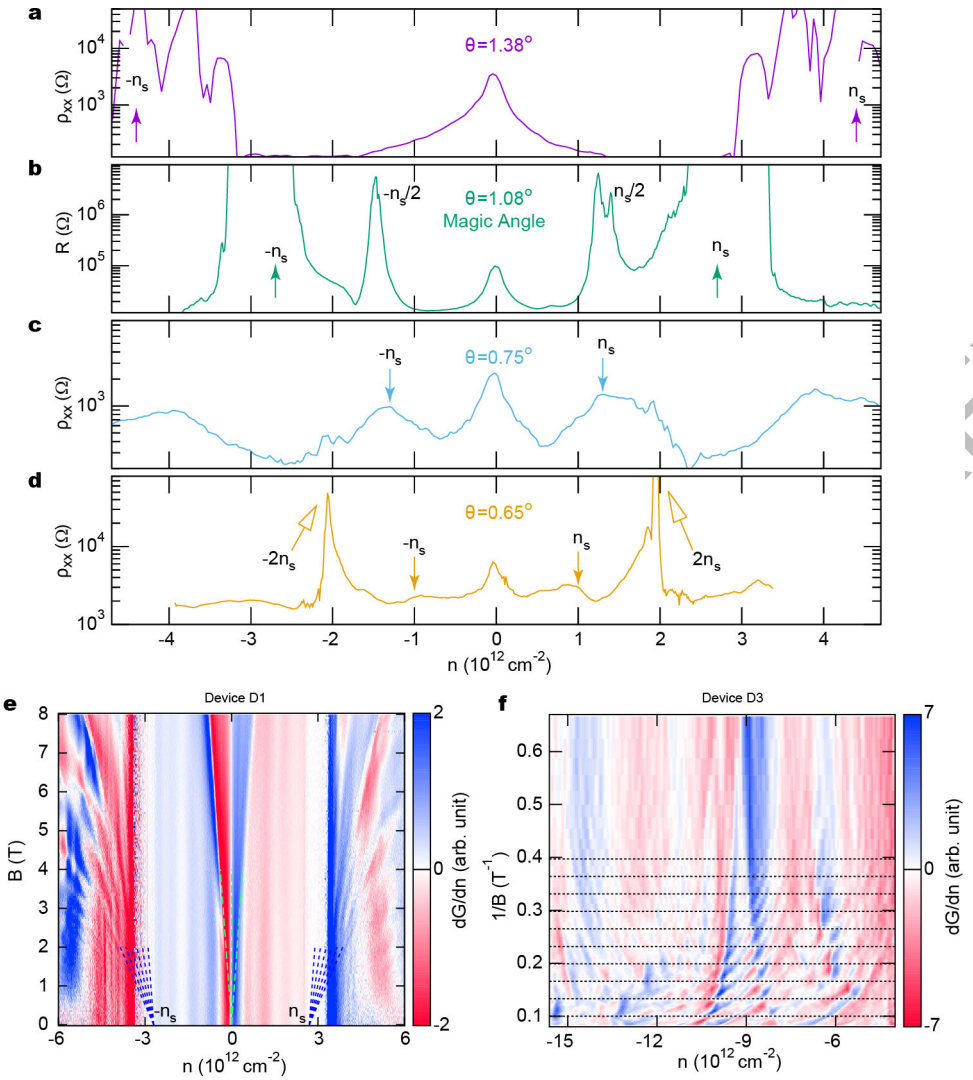

Extended Data Figure 7 | Determination of the twist angle. (a-d) Resistivity (resistance for the $\theta = 1.08°$ device) measurements for four samples with different twist angles, $\theta = 1.38°$, 1.08°, 0.75° and 0.65°. The solid arrows point towards superlattice features at $\pm n_s$, while empty arrows point to $\pm 2n_s$ features that may have correspondence to features reported in Ref. 17. We have only observed the half-filling states in devices that have twist angles within 0.1° of the first magic angle so far. (e) Magnetoconductance data of device D1 ($\theta = 1.08°$) measured at 4 K and taken derivative with respect to n. The dashed fans labels the main (green) and satellite (blue) Landau fans respectively. From the converging point of the blue fans, one can accurately determine the superlattice density n_s and thus θ, with uncertainty of about 0.02°. (f) Hofstadter's oscillation manifested as periodic crossings of Landau levels in $1/B$. Data shown is the magnetoconductance data of device D3 ($\theta = 1.12°$) which is taken first derivative in n. The horizontal lines have a uniform spacing of $0.033 = 0.001\ \mathrm{T}^{-1}$, which converts to $\theta = 1.12° \pm 0.01°$.